Check for updates

Advanced Optical Materials

ADVANCED OPTICAL MATERIALS
www.advopticalmat.de

RESEARCH ARTICLE

Rationalizing the Spatial Charge Distribution Modulation of Carbazole-Based Additives for Efficient Perovskite Quantum Dots Light-Emitting Diodes

Lunyao Pan[1,2] | Xinning Wang[1] | Yuqiang Huang[3] | Xiankan Zeng[1] | Maolin Mu[1] | Junsheng Yu[2] | Weiqing Yang[1,4] | Ding Zheng[2] | Wen Li[1]

[1]Key Laboratory of Advanced Technologies of Materials (Ministry of Education), School of Materials Science and Engineering, Southwest Jiaotong University, Chengdu, People's Republic of China | [2]School of Optoelectronic Science and Engineering, University of Electronic Science and Technology of China, Chengdu, People's Republic of China | [3]School of Materials Science and Engineering, Jilin University, Changchun, People's Republic of China | [4]Research Institute of Frontier Science, Southwest Jiaotong University, Chengdu, People's Republic of China

Correspondence: Junsheng Yu (jsyu@uestc.edu.cn) | Ding Zheng (dingZheng@uestc.edu.cn) | Wen Li (liwen3337@swjtu.edu.cn)

Received: 28 February 2026 | **Revised:** 8 September 2026 | **Accepted:** 14 September 2026

Keywords: carbazole additives | perovskite light-emitting diodes | perovskite quantum dots | spatial charge

ABSTRACT

Achieving efficient perovskite light-emitting diodes (PeLEDs) requires the simultaneous suppression of surface defects and regulation of carrier transport, yet integrating these functions within a single molecular design remains challenging. Here, three carbazole-based molecules were introduced during the synthesis of $FAPbBr_3$ perovskite quantum dots (PQDs). Complementary FTIR and XPS analyses reveal carbazole-derived vibrational features and additive-dependent perturbations of the nitrogen and lead electronic environments, establishing a comparative sequence of molecular association with the PQD surface. Among the three additives, 3,6-bis(9-carbazolyl)-9-methylcarbazole (MCP) exhibits the most negative calculated adsorption energy and the largest N 1s and Pb 4f binding-energy shifts, consistent with the strongest interfacial electronic interaction. This pronounced interfacial interaction is accompanied by the most substantial improvements in the photophysical characteristics of the PQDs and the electroluminescent performance of the resulting PeLEDs. The extended π-conjugated framework further facilitates interfacial charge transport and radiative recombination in green-emissive PeLEDs. As a result, MCP-based PeLEDs exhibit an enhanced peak external quantum efficiency from 11.77% to 19.43%, together with a maximum luminance of 46434 cd/m^2. This work clarifies the molecular-level role of spatial charge distribution in carbazole-based additives and provides a rational guideline for designing multifunctional passivators for green PQD-based PeLEDs.

1 | Introduction

Perovskite quantum dots (PQDs) have emerged as highly promising emissive materials for perovskite light-emitting diodes (PeLEDs), thanks to their remarkable optoelectronic characteristics: tunable bandgaps, high photoluminescence quantum yield (PLQY), a narrow emission peak full-width at half-maximum (FWHM), and facile room temperature solution processability [1–3]. However, PeLEDs still face the issue of carrier transport imbalance, often exhibiting high turn-on voltages and increased Joule heating, which directly leads to reduced device brightness and efficiency. The inherent dynamic equilibrium of surface

Lunyao Pan and Xinning Wang contributed equally to this work.

All rights reserved, including rights for text and data mining and training of artificial intelligence technologies or similar technologies.
© 2026 Wiley-VCH GmbH

ligands of PQDs and the mismatch of device interface properties characteristics are the key factors that hinder the carrier transport equilibrium [4, 5].

Researchers have demonstrated that ligand engineering and interface engineering are effective strategies to address these challenges [6–8]. For ligand engineering, ligand exchange is commonly used to replace long-chain insulating ligands with shorter or more functional ligands, thereby reducing the carrier-transport barrier between neighboring PQDs [4, 9]. Representative Lewis-base ligands, including trioctylphosphine oxide (TOPO) and isopropyl phenylphosphonate (PPIA), can coordinate with undercoordinated Pb^{2+} sites, optimize surface states, and improve carrier mobility [10, 11]. For interface engineering, the insertion of interfacial layers or the modification of charge-transport layers is typically employed to regulate energy-level alignment, reduce injection barriers, and suppress interfacial defects [12, 13]. Nevertheless, ligand engineering and interface engineering are usually implemented separately, which may create a trade-off between surface passivation quality and interfacial charge injection [14–17]. More broadly, phosphorus-containing Lewis-base molecules, particularly phosphine oxides and phosphonates, have been widely explored for Pb-site passivation in perovskite QD and PeLED systems. Their electron-donating P = O or P-O groups can coordinate with undercoordinated Pb^{2+} defects and suppress non-radiative recombination, while conjugated phosphine oxide frameworks may further contribute to interfacial electronic coupling and carrier injection. These studies indicate that coordination-site chemistry and molecular electronic structure are both important for designing efficient passivating additives. Nevertheless, compared with phosphine oxide- and phosphonate-based passivators, carbazole-based additives have been less systematically investigated from the perspective of intramolecular spatial charge distribution, especially when introduced during PQD synthesis to simultaneously regulate surface coordination, defect passivation, energy-level alignment and carrier dynamics [18, 19].

Herein, three distinct carbazole derivatives (N-phenylcarbazole (NPC), 3,6-bis(9-carbazolyl)-9-methylcarbazole (MCP), and 4,4′-bis(N-carbazolyl)-1,1′-biphenyl (CBP)) were selected as multifunctional additives. The electron-rich nitrogen centers and π-conjugated frameworks of these molecules give rise to distinct interactions with the $FAPbBr_3$ QD surface, as reflected by their calculated adsorption energies and additive-dependent spectroscopic responses. Among the three additives, MCP exhibits the strongest interfacial electronic interaction, accompanied by the most pronounced improvements in PQD photophysical properties and device performance. The central novelty of the present work lies not in the simple use of carbazole-containing molecules, but in clarifying how spatial charge distribution and the conjugated molecular framework, together with coordination site accessibility and molecular geometry, influence PQD surface chemistry and the device level electrical response of green PQD-based PeLEDs. Following equal molar concentration optimization, the optimized MCP-F PeLEDs reach an EQE_{max} of 19.43%, an L_{max} of 46434 cd/m^2, and a maximum current efficiency of 81.27 cd/A. This work provides molecular level insight into the coupled electronic and structural factors governing carbazole-PQD interactions and offers guidance for screening efficient multifunctional passivators for PQD-based PeLEDs. Beyond carbazole derivatives, this spatial charge-distribution principle may also provide a useful guideline for other conjugated ligand systems, such as conjugated phosphines and phosphine oxides, in which electron-donating coordination centers can bind undercoordinated Pb^{2+} sites while the conjugated backbone may mediate interfacial charge transport. Nevertheless, the present work focuses on carbazole-based additives; systematic validation of this principle in other ligand families will be the subject of future studies.

2 | Results and Discussion

Ligand-assisted reprecipitation (LARP) is one of the most common synthesis methods for perovskite quantum dots. $FAPbBr_3$ quantum dots were synthesized by injecting the DMF precursor solution containing $PbBr_2$ and FABr into a crystallization-inducing solution composed of toluene, 1-butanol, oleic acid, and oleylamine (OLA) to trigger nucleation (Figure S1). Three carbazole-based additives (NPC, MCP, and CBP) were added to the crystallization-inducing solution, and the resulting $FAPbBr_3$ QDs were denoted as NPC-F, MCP-F, and CBP-F, respectively. An effective guest passivator should perform its function without disrupting the host lattice integrity. X-ray diffraction (XRD) patterns demonstrate that the characteristic diffraction peaks of the perovskite lattice remain unchanged after treatment with the carbazole additives (Figure S2) [20, 21]. Moreover, aggregation of PQDs during the nucleation process is inhibited due to the steric hindrance effect of rigid planar additives. The average particle diameters of the Control, NPC-F, MCP-F, and CBP-F QDs are 13.12, 12.25, 12.21, and 12.32 nm, respectively, indicating that the carbazole additives subtly modulate nanocrystal nucleation and growth (Figure S3) [22, 23].

The three carbazole molecules possess different π-conjugated frameworks (Figure S4), which strongly influence their intramolecular charge separation and electrostatic interaction with PQD surfaces. To visualize these differences, electrostatic potential (ESP) distributions were calculated by density functional theory (DFT) (Figure 1a-c). MCP (μ = 1.344 Debye) exhibits a more asymmetric and delocalized spatial charge distribution than NPC (μ = 0.364 Debye) and CBP (μ = 0.001 Debye). This charge separation creates alternating electropositive and electronegative regions along the molecular framework, providing a favorable electrostatic environment for interfacial association and charge redistribution. Consequently, perovskite/MCP (−2.81 eV) exhibits a more negative adsorption energy than perovskite/NPC (−2.41 eV) and perovskite/CBP (−1.56 eV) (Figure 1d-f). It should be noted that the stronger adsorption of MCP should not be attributed solely to its dipole moment; rather, it arises from the combined contribution of spatial charge distribution, accessible nitrogen coordination sites, conjugation length, and molecular geometry [24]. Electron-density-difference (EDD) analysis further visualizes the interfacial charge redistribution between carbazole additives and the $FAPbBr_3$ surface (Figure S5). The charge accumulation near the Pb-coordination region and charge depletion around the electron-donating carbazole moieties support interfacial charge transfer associated with N-Pb coordination and defect passivation [25, 26]. Notably, the MCP/$FAPbBr_3$ interface exhibits a more pronounced charge-redistribution pattern than the NPC/$FAPbBr_3$ and CBP/$FAPbBr_3$ interfaces, with stronger

21951071, 2026, 38, Downloaded from https://advanced.onlinelibrary.wiley.com/doi/10.1002/adom.71833 by Jilin University, Wiley Online Library on [07/11/2026]. See the Terms and Conditions (https://onlinelibrary.wiley.com/terms-and-conditions) on Wiley Online Library for rules of use; OA articles are governed by the applicable Creative Commons License

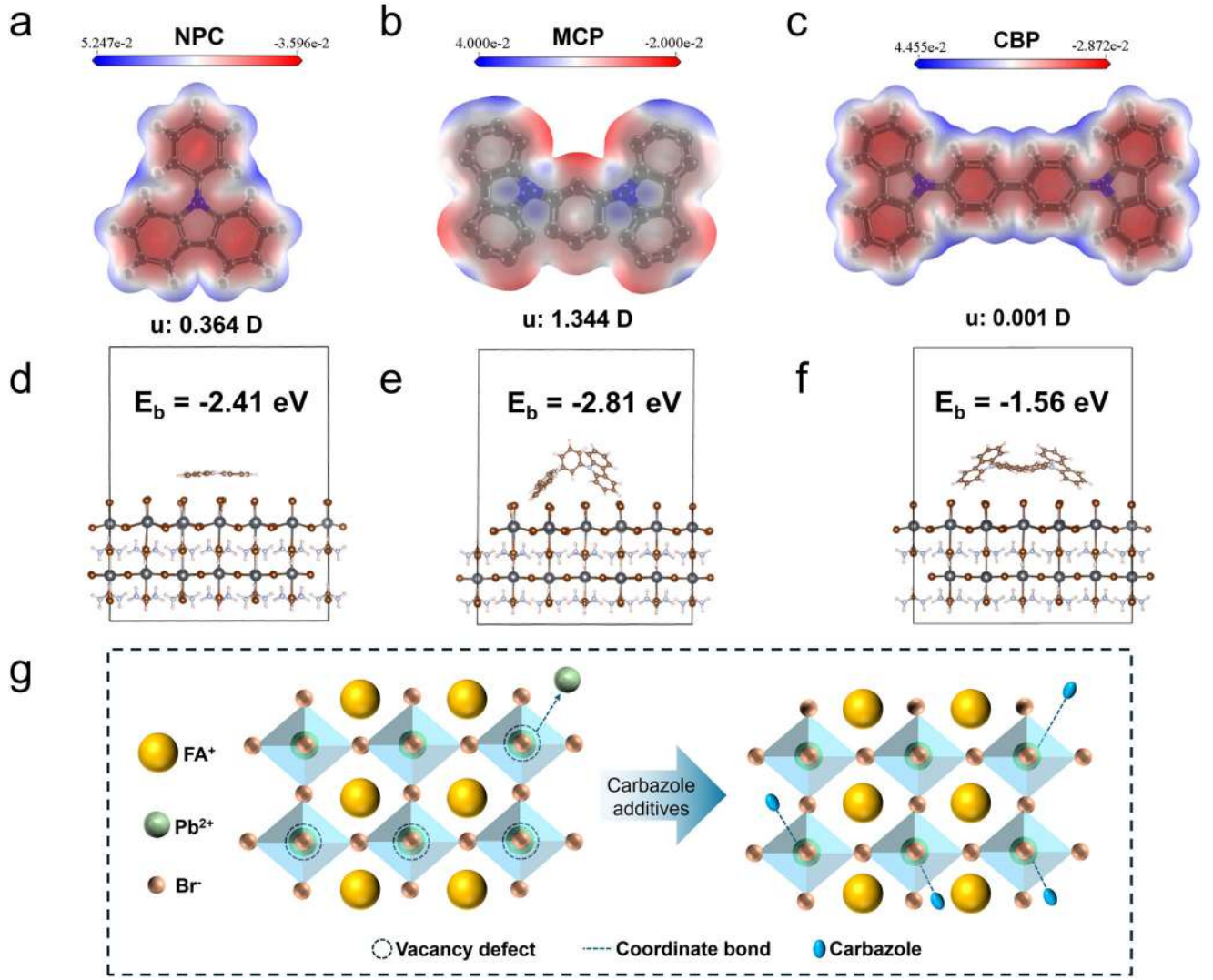


FIGURE 1 | Schematic illustration of the theoretical calculation results. (a-c) ESP analysis of NPC, MCP, and CBP. (d-f) Adsorption configurations and binding energies (E_b) of NPC, MCP, and CBP on the $FAPbBr_3$ perovskite surface. (g) Schematic diagram of carbazole-assisted passivation of perovskite surface defects.

electron accumulation and depletion localized around the Pb-coordination region and the carbazole framework. This enhanced interfacial charge transfer is consistent with the larger adsorption energy, the N 1s chemical shift, and the Pb 4f binding-energy shift, suggesting stronger electronic coupling and more effective defect passivation in the MCP-F system.

FTIR spectroscopy was employed to probe the interaction between the carbazole additives and the purified PQDs. The additive-treated samples retain the characteristic C = C asymmetric stretching bands near 1505 and 1602 cm^{-1}, while their slight shifts relative to the corresponding molecular references indicate a modified local electronic environment upon association with the PQDs (Figure 2a and Figure S6) [27]. Complementary XPS measurements reveal additive-dependent changes in the Pb 4f and Br 3d binding energies (Figure 2b, c). The Pb 4f peaks shift toward lower binding energy by 0.02, 0.04, and 0.10 eV for CBP-F, NPC-F, and MCP-F, respectively, indicating a progressively stronger perturbation of the Pb electronic environment [11, 28]. The coordinated FTIR and XPS responses therefore establish the relative interfacial interaction sequence CBP-F < NPC-F < MCP-F.

To further confirm the nitrogen-assisted coordination mechanism, N 1s XPS spectra were collected for pristine carbazole molecules and carbazole-modified PQD films (Figure S7). The pure NPC, MCP and CBP molecules exhibit characteristic carbazole-related N 1s peaks, whereas the modified PQD films contain contributions from both FA-related nitrogen in $FAPbBr_3$ and carbazole-related nitrogen in the additives. Compared with the corresponding pristine carbazole molecules, the carbazole-related N 1s components of NPC-F and MCP-F shift toward higher binding energy by 0.12 and 0.27 eV, respectively, indicating decreased electron density around the nitrogen centers after interaction with undercoordinated Pb^{2+} sites. By contrast, CBP-F shows a negligible shift of 0.01 eV, suggesting a much weaker electronic interaction with the PQD surface. This trend is consistent with the Pb 4f shift and calculated adsorption tendency, further supporting the stronger N-Pb electronic interaction in MCP-F.

21951071, 2026, 38, Downloaded from https://advanced.onlinelibrary.wiley.com/doi/10.1002/adom.71833 by Jilin University, Wiley Online Library on [07/11/2026]. See the Terms and Conditions (https://onlinelibrary.wiley.com/terms-and-conditions) on Wiley Online Library for rules of use; OA articles are governed by the applicable Creative Commons License

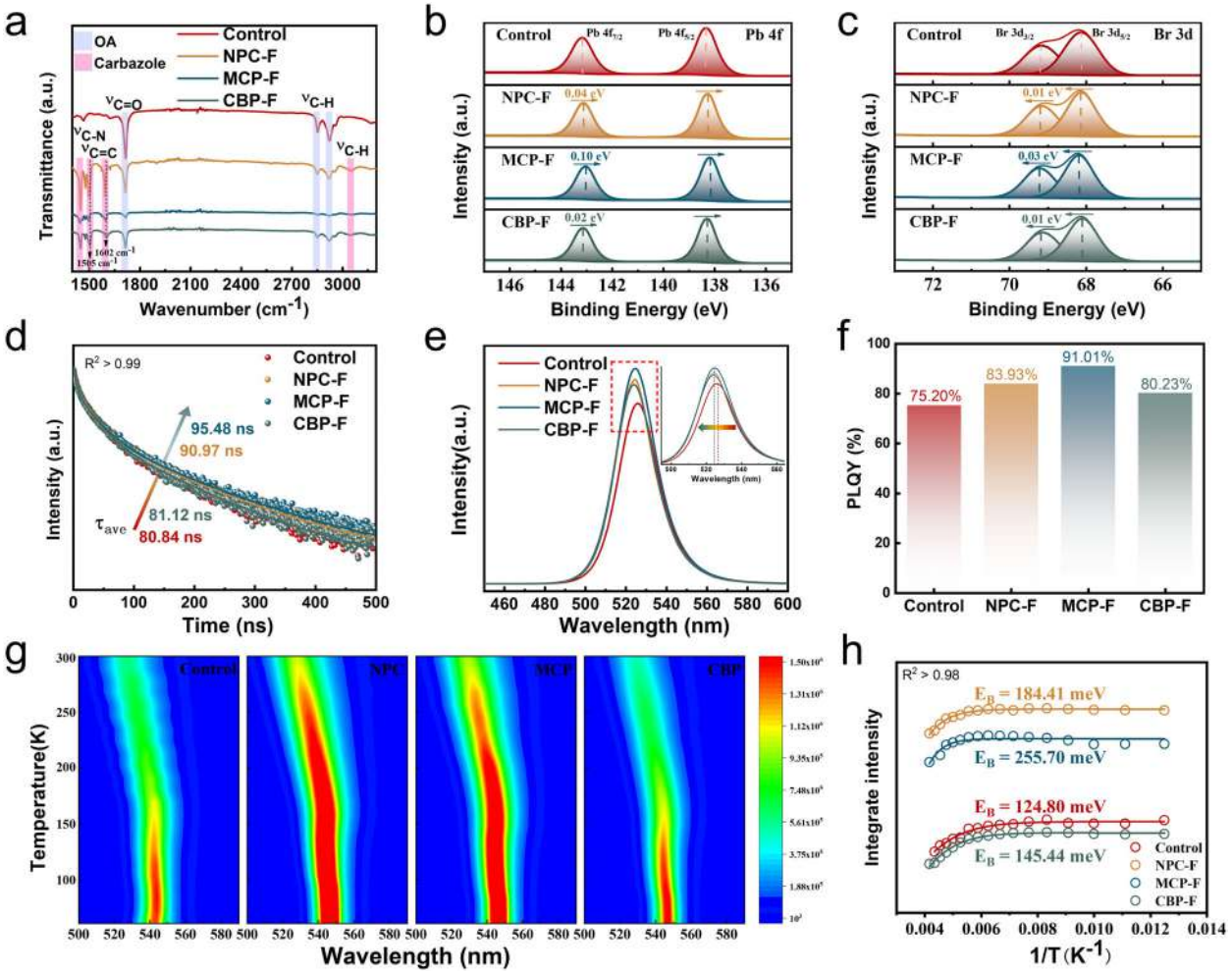


FIGURE 2 | Photophysical properties of PQDs. (a) FTIR spectra, (b) Pb 4f, (c) Br 3d XPS spectra, (d) TRPL spectra, (e) PL spectra, (f) PLQY, (g) 2D temperature-dependent PL spectra of Control, NPC-F, MCP-F and CBP-F perovskite films. (h) Integrated PL intensity as a function.

To evaluate the photophysical properties of the emission layer (EML), comprehensive measurements including time-resolved photoluminescence (TRPL), photoluminescence (PL) and Photoluminescence Quantum Yield (PLQY) were conducted (Figure 2d-f and Table S1). Relative to the Control film, which exhibits an average lifetime of 80.84 ns and a PLQY of 75.20%, the corresponding values increase to 81.12 ns and 80.23% for CBP-F, 90.97 ns and 83.93% for NPC-F, and 95.48 ns and 91.01% for MCP-F, respectively. Compared with the Control, all additive-treated films exhibit enhanced PL emission accompanied by a modest blue shift. The concomitant reduction in nanocrystal dimensions is consistent with an increase in the band-edge transition energy arising from strengthened quantum confinement. Meanwhile, the progressive increases in PLQY and average lifetime indicate increasingly suppressed nonradiative decay, with MCP-F exhibiting the most pronounced improvement [29, 30]. Temperature-related PL spectra were employed to investigate the exciton dynamics in perovskite films. The data extracted from the 2D (Figure 2g) and 3D (Figure S8) spectral profiles were well fitted ($R^2 > 0.98$). The exciton binding energy (E_B) was calculated using the Arrhenius equation [31, 32]:

$$I\ (T) = \frac{I_0}{1 + Ae^{[-E_B/k_BT)}}$$

where I_0 is the PL integral intensity at temperature T_0, and A is the proportionality coefficient. E_B represents the energy required for excitons to dissociate into free electron and hole charge carriers at room temperature, and k_B is the Boltzmann constant. A larger E_B indicates higher barrier for exciton dissociation [33]. In Figure 2h, E_B increased from 124.80 meV (Control) to 255.70 meV (MCP-F), demonstrating that coordination-mediated and π-conjugation-assisted carbazole additives effectively passivate Pb-related defects and reduce non-radiative recombination centers in QDs. Space charge limited current (SCLC) further estimated the trap density of $FAPbBr_3$ films (Figure S9), and the MCP-F-based hole-only device (HOD) possessed the lowest trap-filling limiting voltage (V_{TFL}) of 0.78 V, outperforming those based on NPC-F (0.83 V), CBP-F (0.88 V), and Control (0.92 V). The trap density (n_t) of PQDs is estimated by the equation $n_t = 2\varepsilon\varepsilon_0 V_{TFL}/eL^2$ [34], where e is the basic charge, L is the thickness of the EML layer, ε_0 and ε are the vacuum dielectric constant and relative dielectric constant, respectively. Based on above equation, we calculated the trap density of MCP-F is $1.83\times10^{17}cm^{-3}$, which is lower than NPC-F ($1.95\times10^{17}cm^{-3}$), CBP-F ($2.1\times10^{17}cm^{-3}$), and Control ($2.2\times10^{17}cm^{-3}$). To complement the HOD results and evaluate carrier balance, electron-only device (EOD) was further fabricated to assess the electron-injection characteristics of the modified PQD films (Figure S10) [15]. Together with the enhanced

21951071, 2026, 38, Downloaded from https://advanced.onlinelibrary.wiley.com/doi/10.1002/adom.71833 by Jilin University, Wiley Online Library on [07/11/2026]. See the Terms and Conditions (https://onlinelibrary.wiley.com/terms-and-conditions) on Wiley Online Library for rules of use; OA articles are governed by the applicable Creative Commons License

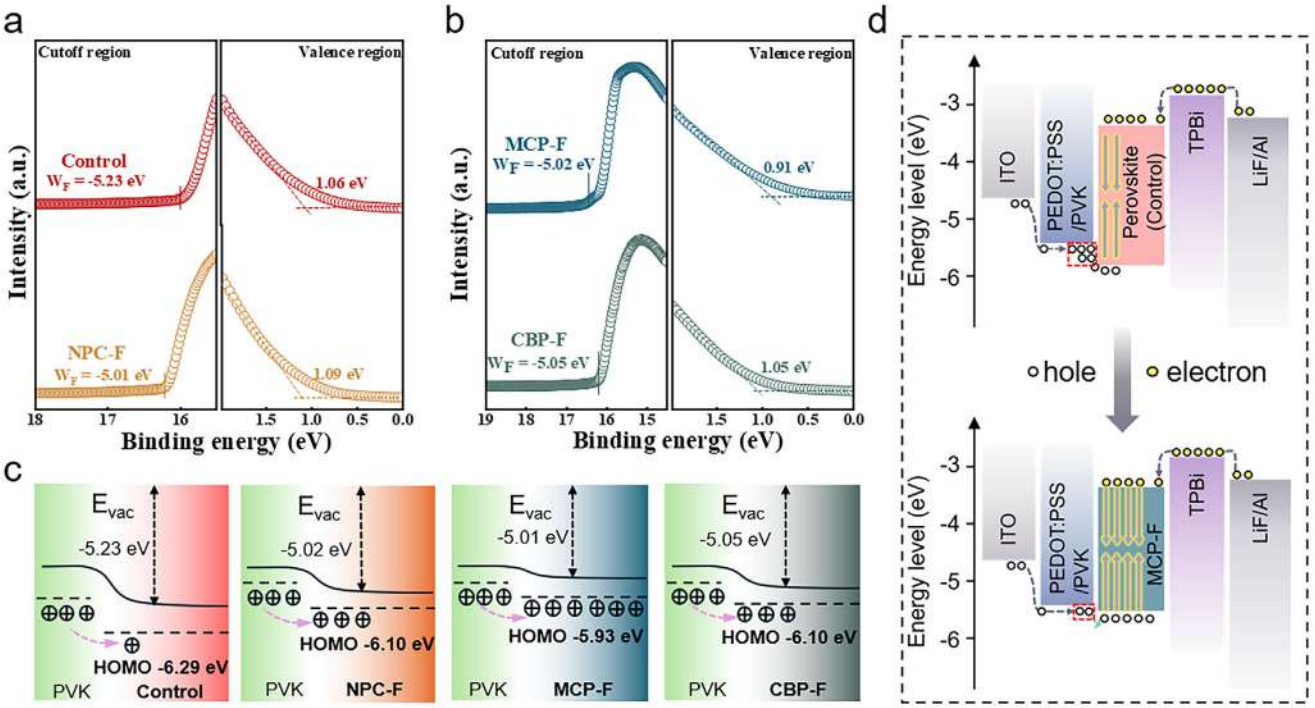


FIGURE 3 | (a, b) UPS spectra of secondary electron cut-off and valence bands of Control, NPC-F, MCP-F and CBP-F perovskite. (c) The schematic diagrams of hole injection at PVK/$FAPbBr_3$ interfaces. (d) Schematic diagram of carrier radiation recombination.

PLQY and prolonged lifetime, the lower V_{TFL} and trap density of MCP-F are consistent with a reduced contribution from trap-assisted recombination and a more balanced single-carrier response.

Ultraviolet photoelectron spectroscopy (UPS) was employed to probe the influence of spatial charge distribution of carbazole-based additives on the band structure of PQDs. By analyzing the secondary cutoff edges and valence band regions shown in Figure 3a,b, we found that the hole injection barriers based on MCP-F, NPC-F, and CBP-F PQDs were reduced by 0.36 eV, 0.19 eV, and 0.19 eV, respectively, compared to control PQDs (Figure 3c). The larger dipole moment of MCP promotes the formation of a stronger surface electric field via coordination between the electron-rich nitrogen centers of the carbazole groups and uncoordinated Pb^{2+} ions on the PQDs surface. This leads to a more pronounced upward bending of the HOMO energy level and a reduced hole injection barrier at the PVK/MCP-F interface, which facilitates the radiative recombination of electron and hole in the EML (Figure 3d) [35].

We fabricated devices with a structure of ITO/PEDOT /PVK/$FAPbBr_3$/TPBi/LiF/Al and semi-quantitatively evaluated variations of the interfacial carrier accumulation and recombination behaviors by capacitance-voltage (*C-V*) measurements [36]. The characteristic capacitance decreases shifts from 5.34 V for the Control device to 4.84, 4.62, and 2.66 V for CBP-F, NPC-F, and MCP-F, respectively (Figure 4a). The MCP-F device also displays the most negative d*C*/d*V* response of -2.27 nF V^{-1} and reaches a stable capacitance regime at a lower characteristic frequency (Figures S11 and S12). Collectively, these features are consistent with an earlier evolution from interfacial charge storage toward recombination-dominated operation under forward bias, in agreement with the modified electronic environment of the MCP-F emissive layer.

Broadband impedance-magnitude and phase-angle measurements were further employed to compare the voltage- and frequency-dependent electrical responses of the four PeLEDs [37, 38]. At 10^4 Hz, the impedance of the MCP-F device decreases from 5.2×10^7 Ω at 0 V to 253 Ω at 6.5 V, whereas those of the NPC-F and CBP-F devices decrease from 8.2×10^6 to 475 Ω and from 7.3×10^4 to 374 Ω, respectively, under the same conditions (Figure 4b) [39, 40]. The pronounced voltage induced decrease in the effective impedance of MCP-F is consistent with more favorable carrier injection and transport under forward bias. The Nyquist spectra, acquired separately over 0.1 Hz to 1 MHz, provide a complementary comparison of the small signal electrical response under identical operating conditions (Figure 4c) [41]. In the phase-angle maps, the characteristic transition voltage at 10^3 Hz decreases to 2.3 V for MCP-F, compared with 3.4, 3.5, and 3.7 V for the Control, NPC-F, and CBP-F devices, respectively (Figure 4d). This lower transition voltage agrees with the reduced hole-injection barrier obtained from UPS. At higher frequencies, the diminished contribution of slower interfacial polarization processes is accompanied by a broader voltage-dependent phase and reactance response for MCP-F (Figure S13) [42, 43].

The PeLEDs adopt an ITO/PEDOT:PSS/PVK/$FAPbBr_3$/TPBi/LiF/Al structure (Figure 5a). To minimize the influence of unequal molecular loading associated with the different molecular weights of NPC, MCP, and CBP, concentration dependent device measurements were additionally performed using identical nominal additive concentrations of 0.01, 0.02, and 0.03 M (Figure S14). All three additive systems exhibit their highest overall device performance at 0.02 M. Minor variations in absolute

21951071, 2026, 38, Downloaded from https://advanced.onlinelibrary.wiley.com/doi/10.1002/adom.71833 by Jilin University, Wiley Online Library on [07/11/2026]. See the Terms and Conditions (https://onlinelibrary.wiley.com/terms-and-conditions) on Wiley Online Library for rules of use; OA articles are governed by the applicable Creative Commons License

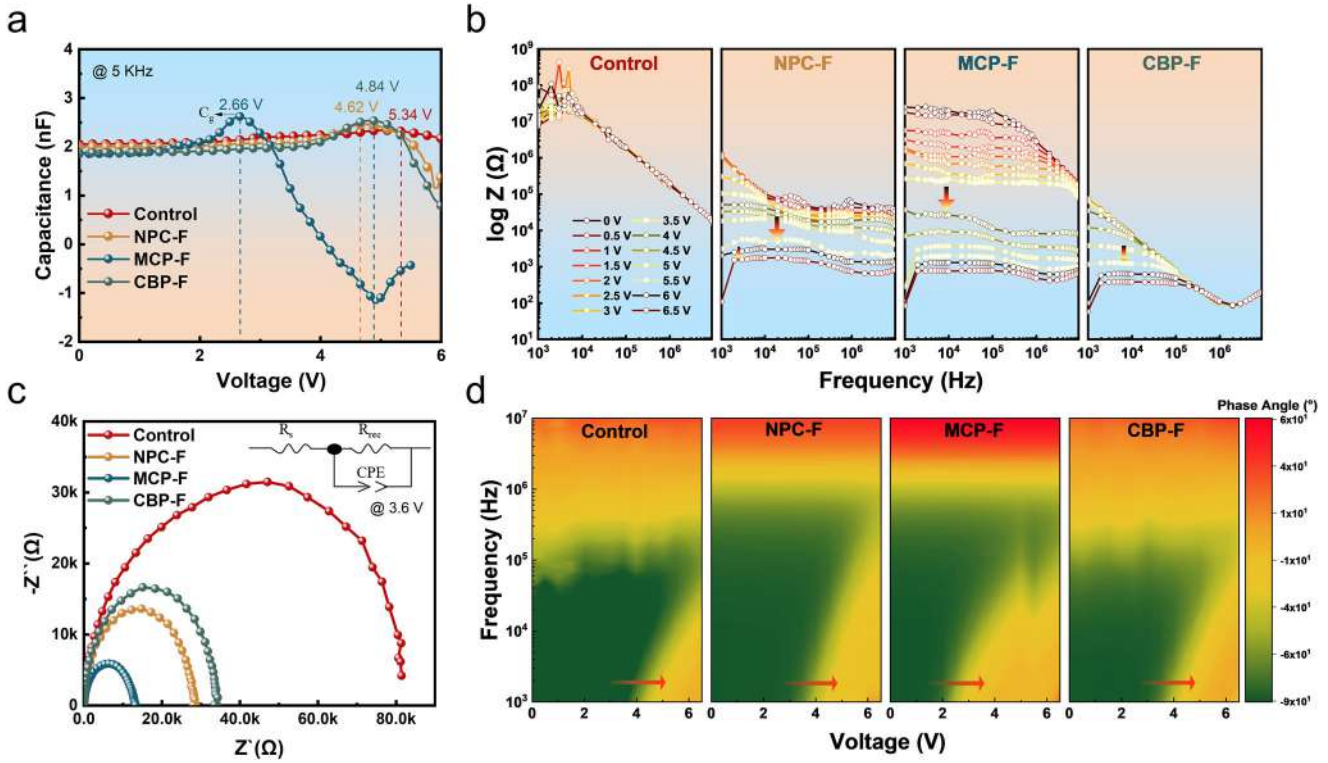


FIGURE 4 | Electrical response characteristics of the PeLEDs. (a) Capacitance-voltage characteristics measured at 5 kHz. (b) Voltage-dependent impedance magnitude measured at selected frequencies within 10^3–10^7 Hz. (c) Nyquist spectra acquired over 0.1 Hz-1 MHz. (d) Frequency-voltage phase-angle maps acquired over 10^3–10^7 Hz for the Control, NPC-F, MCP-F, and CBP-F PeLEDs.

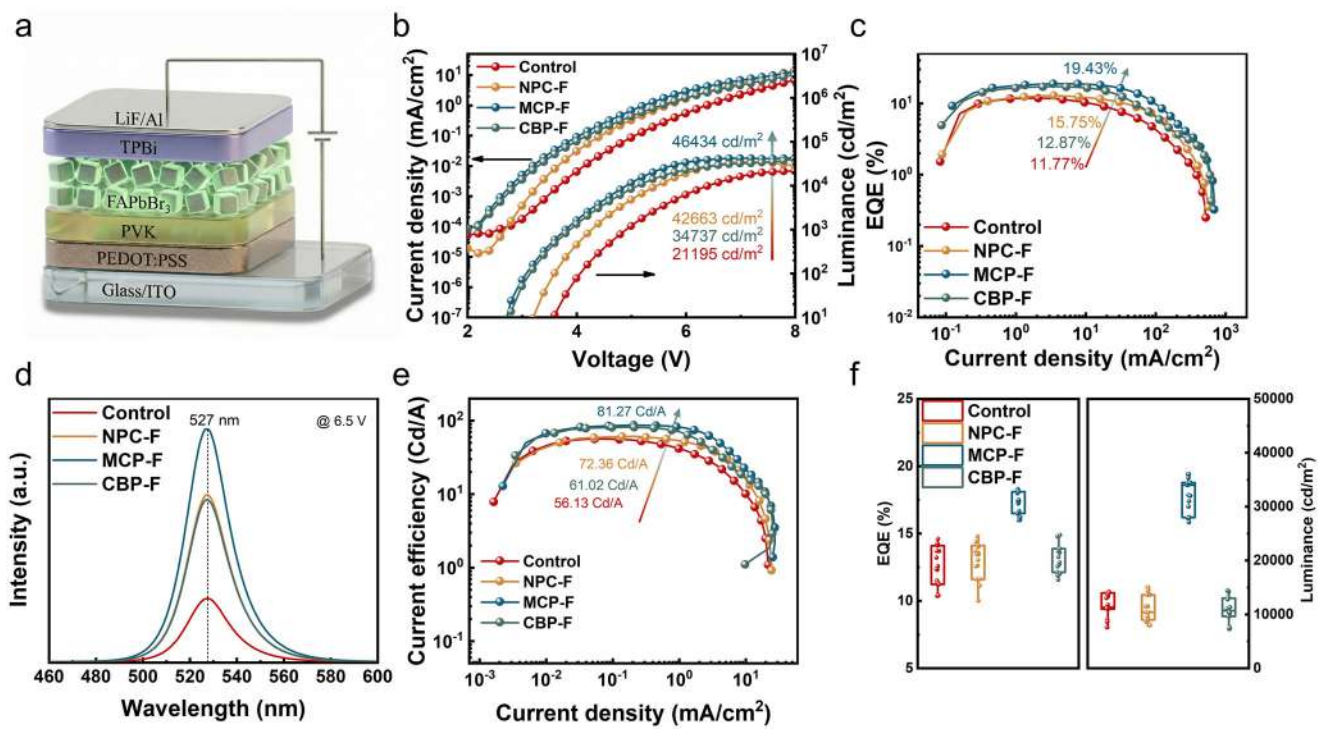


FIGURE 5 | Device structure and electroluminescent performance of PeLEDs under the optimized equal-molar additive condition. (a) Schematic device architecture. (b) Current density-luminance-voltage (*J-L-V*) characteristics of Control, NPC-F, MCP-F, and CBP-F PeLEDs, with the additive-modified devices prepared at the optimized concentration of 0.02 M. (c) External quantum efficiency-current density (EQE-*J*) characteristics. (d) EL spectra measured at 6.5 V. (e) Current efficiency-current density (*CE-J*) characteristics. (f) Statistical distributions of EQE_{max} and L_{max} for the four device groups. Individual data points are overlaid on the distributions.

21951071, 2026, 38, Downloaded from https://advanced.onlinelibrary.wiley.com/doi/10.1002/adom.71833 by Jilin University, Wiley Online Library on [07/11/2026]. See the Terms and Conditions (https://onlinelibrary.wiley.com/terms-and-conditions) on Wiley Online Library for rules of use; OA articles are governed by the applicable Creative Commons License

device metrics were observed among independently fabricated batches, which are reasonably associated with batch-dependent variations in precursor conditions and solution-processing parameters. Importantly, the relative performance hierarchy remained consistent across the independently prepared devices, demonstrating the robustness of the comparative performance trend. Accordingly, 0.02 M was selected as the common optimized concentration for the representative additive-modified devices compared in Figure 5. At the optimized equal-molar concentration of 0.02 M, the representative MCP-F device exhibits the highest electroluminescent performance, reaching an EQE_{max} of 19.43% and an L_{max} of 46434 cd/m^2, compared with 11.77% and 21195 cd/m^2 for the Control device (Figure 5b, c). Under the same optimized loading condition, NPC-F and CBP-F exhibit EQE_{max} values of 15.75% and 12.87%, with corresponding L_{max} values of 42663 and 34737 cd/m^2, respectively. All four devices retain narrow green electroluminescence centered at approximately 527 nm at 6.5 V (Figure 5d). The maximum current efficiencies follow the same overall performance hierarchy, increasing from 56.13 cd/A for the Control to 61.02, 72.36, and 81.27 cd/A for CBP-F, NPC-F, and MCP-F, respectively (Figure 5e). Device to device reproducibility was further evaluated from the statistical distributions of EQE_{max} and L_{max} shown in Figure 5f, with the corresponding mean values, standard deviations, and measured ranges summarized in Table S2. Importantly, the superior performance of MCP-F is retained after normalizing the additive loading on an identical molar basis, indicating that the observed performance advantage cannot be attributed simply to the different numbers of additive molecules introduced under the original equal-mass condition. Nevertheless, because NPC, MCP, and CBP also differ in coordination-site accessibility, conjugation length, molecular geometry, and steric environment, the observed device hierarchy is attributed to their combined molecular electronic and structural characteristics rather than to spatial charge distribution alone. Taken together, these results indicate that spatial charge distribution, coordination site accessibility, and the conjugated molecular framework act cooperatively in regulating PQD surface passivation and device level carrier transport. Operational stability was further evaluated by monitoring luminance decay under a fixed initial luminance or constant-current driving condition, and the T_{50} values of Control, NPC-F, MCP-F, and CBP-F devices are 3.26 min, 5.63 min, 6.11 min, and 5.41 min, respectively (Figure S15). The prolonged T_{50} lifetime of the MCP-F device indicates improved operational robustness, which is consistent with the more effective Pb-related defect passivation and reduced non-radiative recombination enabled by the stronger interfacial electronic interaction between MCP and the PQD surface. In addition, voltage-dependent EL spectra were collected to examine the spectral stability of the modified devices (Figure S16) [44, 45]. The optimization strategy based on carbazole-based additives significantly enhanced the performance of $FA_{0.85}GA_{0.15}PbBr_3$ QD-based LEDs, demonstrating the broad applicability of this spatial charge regulation approach in improving the performance of PQDs-based LEDs (Figure S17).

3 | Conclusions

In summary, we investigated the influence of spatial charge regulation in carbazole-based additives on the photophysical properties of PQDs and the carrier dynamics of PeLEDs. Within the investigated molecular series, MCP exhibits the most negative adsorption energy and the largest N 1s and Pb 4f binding-energy shifts, collectively identifying the strongest interfacial electronic interaction among the three carbazole additives. The modest blue shift of the additive-treated PQDs follows the accompanying reduction in nanocrystal dimensions, consistent with the size-dependent band-edge structure of $FAPbBr_3$ QDs. The coordinated increases in PLQY and carrier lifetime, together with the reductions in V_{TFL} and trap density, reveal progressively suppressed trap-assisted nonradiative recombination, with MCP-F exhibiting the most pronounced improvement. Consequently, the optimized pure-green MCP-F PeLEDs prepared at an additive concentration of 0.02 M achieve an EQE_{max} of 19.43%, an L_{max} of 46434 cd/m^2, and a maximum current efficiency of 81.27 cd/A, while retaining narrow green electroluminescence centered at approximately 527 nm. This work combines theoretical calculations and experimental characterization to establish a molecular-level connection between PQD surface modification and interfacial carrier transport. More importantly, these findings suggest a molecular design principle in which spatial charge distribution, coordination capability, and conjugated-framework-mediated transport are considered together. This principle may be extended to other conjugated ligand systems, but broader validation beyond carbazole derivatives remains an important direction for future studies.

4 | Experimental Section

4.1 | Materials

Lead bromide ($PbBr_2$, 99%) and iso-propyl alcohol ($(CH_3)_2CHOH$) were obtained from Shanghai Macklin Co., Ltd. Ethanol, toluene (99.9%), octane (98%), and N, N-dimethylformamide (DMF, 98%) were provided by Keshi. Molybdenum trioxide (MoO_3, 99.95%), oleylamine (OLA, 90%), oleic acid (OA, 90%), toluene (99.9%), and LiF were purchased from Shanghai Aladdin Industrial Corporation Co., Ltd. Formamidinium bromide (FABr, 99.5%), guanidinium bromide (GABr, 99.5%), 2,2′,2″-(1,3,5-benzinetriyl)-tris(1-phenyl-1H-benzimidazole) (TPBi, 99.9%), poly(9-vinylcarbazole) (PVK), PEDOT:PSS (Clevios Al 4083), N-phenylcarbazole (NPC, 99.5%), 3,6-bis(9-carbazolyl)-9-methylcarbazole (MCP, 99.5%), and 4,4′-bis(N-carbazolyl)-1,1′-biphenyl (CBP, 99.5%) were supplied by Xi'an Polymer Light Technology Corp.

4.2 | Preparation of $FAPbBr_3$ QDs

The synthesis of $FAPbBr_3$ QDs was carried out using a modified method based on the literature [46]. The $FAPbBr_3$ precursor (150 µL), prepared by dissolving $PbBr_2$ and FABr in DMF with a molar ratio of 1:2.2 and a Pb^{2+} concentration of 0.2 M, was injected into a vial containing a crystallization-inducing solution composed of 5 mL of toluene, 2 mL of 1-butanol, 500 µL of oleic acid, 30 µL of OLA, and the specified carbazole additive. For the additional equal molar concentration dependent device measurements, NPC, MCP, and CBP were introduced at nominal concentrations of 0.01, 0.02, and 0.03 M while all other synthesis and purification parameters were maintained unchanged. The

21951071, 2026, 38, Downloaded from https://advanced.onlinelibrary.wiley.com/doi/10.1002/adom.71833 by Jilin University, Wiley Online Library on [07/11/2026]. See the Terms and Conditions (https://onlinelibrary.wiley.com/terms-and-conditions) on Wiley Online Library for rules of use; OA articles are governed by the applicable Creative Commons License

0.02 M condition was selected for the optimized additive modified PeLEDs shown in Figure 5. The nominal additive concentration was defined with respect to the 5 mL toluene component of the crystallization-inducing solution. The solution was vigorously stirred for 10 min after injection, followed by centrifugation at 13000 rpm for 5 min, and the supernatant was discarded. The precipitate was redispersed in 1 mL of n-hexane and then centrifuged at 2000 rpm for 2 min. The resulting supernatant was filtered through a 0.22 μm PTFE filter to collect $FAPbBr_3$ QDs. Prior to precursor injection, the crystallization-inducing solution was precooled to 8–10°C. The $FA_{0.85}GA_{0.15}PbBr_3$ precursor (150 μL) was prepared by dissolving $PbBr_2$, FABr, and GABr in DMF with a molar ratio of 7:1:4 and a Pb^{2+} concentration of 0.2 M. The parameters for $FA_{0.85}GA_{0.15}PbBr_3$ QD synthesis remained unchanged, and the laboratory temperature was approximately 28°C.

4.3 | Device Fabrication

$FAPbBr_3$/$FA_{0.85}GA_{0.15}PbBr_3$(FG) QDs were spin-coated at 1000 rpm for 60 s on the PVK films and then quickly transferred into a high-vacuum evaporator without annealing. Subsequently, 50 nm TPBi, 1 nm LiF, and 80 nm Al were sequentially deposited under a low-vacuum environment of 8×10^{-5} Pa. The hole-only devices were fabricated by sequentially depositing 3 nm MoO_3 and 80 nm Ag onto the perovskite films. The electron-only devices were fabricated by sequentially depositing 40 nm TPBi and 80 nm Ag onto the perovskite films.

4.4 | Characterizations

The crystalline structure and quality of $FAPbBr_3$ QD films were investigated by X-ray diffraction (XRD; X'Pert Pro X-ray diffractometer) using Cu Kα radiation (λ = 1.5418 Å). PL, TRPL, and temperature-dependent PL spectra were collected using an FLS980 spectrometer (Edinburgh Instruments) with a 450 W xenon lamp. The room-temperature absolute PLQY values of the films were measured using an Edinburgh FLS980 spectrometer equipped with an integrating sphere. Fourier transform infrared (FTIR) spectra were obtained using a TENSOR II spectrometer (Bruker) with a spectral resolution of 4 cm^{-1}. X-ray photoelectron spectroscopy (XPS) analysis, including Pb 4f, Br 3d, and N 1s spectra, was performed on a Thermo Scientific ESCALAB 250 Xi system. Ultraviolet photoelectron spectroscopy (UPS) measurements were carried out at room temperature using a He discharge lamp (He I, 21.2 eV) as the excitation source in normal emission with a resolution of 0.06 eV on an ESCALAB 220iXL spectrometer. Capacitance-voltage measurements of the PeLEDs were performed at 5 kHz using a Keithley 4200 system. Nyquist impedance spectra were acquired over 0.1 Hz-1 MHz, whereas the impedance-magnitude and phase-angle frequency-voltage maps were collected separately over 10^3–10^7 Hz. The performance of PeLEDs was characterized in a glovebox using a Keithley 2400 source meter combined with a QE-Pro spectrometer (Ocean Optics), and the EL intensity was measured using a FOIS-1 integrating sphere. Operational stability and voltage-dependent EL spectra were recorded to evaluate luminance and spectral stability.

4.5 | Computational Details

The molecular structures of carbazole-based additives were optimized by density functional theory (DFT) using the B3LYP functional and 6–31G (d, p) basis set in the Gaussian 16 software package. The electrostatic surface potential (ESP) distributions of the carbazole-based additives were computed and visualized using Multiwfn 3.8. To examine the binding energy of the carbazole/perovskite interfaces, carbazole molecules were randomly placed on a $5 \times 5 \times 2$ supercell of $FAPbBr_3$, and the interfaces were optimized using the Quickstep code of the CP2K package. The Perdew-Burke-Ernzerhof (PBE) exchange-correlation functional with the DZVP-MOLOPT-SR basis set was used, and dispersion interactions were considered using the DFT-D3 method. EDD maps were calculated from the optimized interface models to visualize charge redistribution upon molecular adsorption, where charge accumulation and depletion regions were used to identify interfacial charge-transfer pathways associated with N-Pb coordination.

Author Contributions

Lunyao Pan: conceptualization, investigation, methodology, validation, software, formal analysis, data curation, supervision, resources, project administration, visualization, Writing – review and editing, funding acquisition, Writing – original draft. **Xinning Wang**: conceptualization, methodology, software, data curation, supervision, resources, project administration, formal analysis, visualization, validation, writing – review and editing, investigation, funding acquisition, writing – original draft. **Yuqiang Huang**: conceptualization, investigation, funding acquisition, validation, visualization, methodology, software, formal analysis, project administration. **Xiankan Zeng**: software, formal analysis, project administration, methodology, validation, visualization, conceptualization, investigation, funding acquisition. **Maolin Mu**: conceptualization, investigation, funding acquisition, methodology, validation. **Junsheng Yu**: conceptualization, investigation, funding acquisition, writing – original draft, writing – review and editing, visualization, formal analysis, project administration, resources, supervision, validation, methodology. **Weiqing Yang**: conceptualization, investigation, funding acquisition, writing – original draft, writing – review and editing, visualization, project administration, supervision, formal analysis, resources, validation. **Ding Zheng**: conceptualization, investigation, funding acquisition, writing – original draft, writing – review and editing, visualization, validation, project administration, formal analysis, resources, supervision, methodology. **Wen Li**: writing – review and editing, visualization, validation, methodology, conceptualization, investigation, funding acquisition, writing – original draft, project administration, formal analysis, resources, supervision.

Acknowledgements

This work was supported by the National Natural Science Foundation of China (No. 52202188), and Supported by the Southwest Jiaotong University Supporting. The authors would like to thank the Analysis and Testing Center of Southwest Jiaotong University for supporting the XRD measurements.

Conflicts of Interest

The authors declare no conflicts of interest.

Data Availability Statement

The data that support the findings of this study are available from the corresponding author upon reasonable request.

21951071, 2026, 38, Downloaded from https://advanced.onlinelibrary.wiley.com/doi/10.1002/adom.71833 by Jilin University, Wiley Online Library on [07/11/2026]. See the Terms and Conditions (https://onlinelibrary.wiley.com/terms-and-conditions) on Wiley Online Library for rules of use; OA articles are governed by the applicable Creative Commons License

References

1. S. A. Veldhuis, P. P. Boix, N. Yantara, et al., "Perovskite Materials for Light-Emitting Diodes and Lasers," *Advanced Materials* 28, no. 32 (2016): 6804–6834.

2. A. Fakharuddin, M. K. Gangishetty, M. Abdi-Jalebi, et al., "Perovskite Light-Emitting Diodes," *Nature Electronics* 5, no. 4 (2022): 203–216.

3. H. Bhatia, B. Ghosh, and E. Debroye, "Colloidal $FAPbBr_3$ Perovskite Nanocrystals for Light Emission: What's Going on?," *Journal of Materials Chemistry C* 10, no. 37 (2022): 13437–13461.

4. Y.-H. Kim, G.-H. Lee, Y.-T. Kim, et al., "High Efficiency Perovskite Light-Emitting Diodes of Ligand-Engineered Colloidal Formamidinium Lead Bromide Nanoparticles," *Nano Energy* 38 (2017): 51–58.

5. D.-H. Kim, S.-J. Woo, C. P. Huelmo, et al., "Surface-Binding Molecular Multipods Strengthen the Halide Perovskite Lattice and Boost Luminescence," *Nature Communications* 15, no. 1 (2024): 6245.

6. Y. Bai, M. Hao, S. Ding, P. Chen, and L. Wang, "Surface Chemistry Engineering of Perovskite Quantum Dots: Strategies, Applications, and Perspectives," *Advanced Materials* 34, no. 4 (2022): 2105958.

7. L. Xu, G. Liu, H. Xiang, et al., "Charge-Carrier Dynamics and Regulation Strategies in Perovskite Light-Emitting Diodes: From Materials to Devices," *Applied Physics Reviews* 9, no. 2 (2022): 021308.

8. S. Yang, M. Moslempoor, X. Li, et al., "Balancing Multiple Properties of Small Molecule Hole-Transporting Materials Towards Highly Efficient Perovskite QLEDs," *Chemical Engineering Journal* 500 (2024): 157117.

9. H. P. Liu, T. R. Li, and Y. H. Wang, "2-Bromohexadecanoic Acid as a Novel Bidentate Ligand for Passivation of Cesium Lead Halide Perovskite Nanocrystals With Near-Unity Photoluminescence Quantum Yield and Superior Photostability," *ACS Applied Materials & Interfaces* 17, no. 16 (2025): 24146–24156.

10. Y. Luo, S. Wang, W. Li, et al., "Dual Ligand Strategy to Manipulate Growth Kinetics of $FAPbBr_3$ Nanocrystals for High-Performance Light-Emitting Diodes," *Small Methods* 9, no. 10 (2025): 2401694.

11. W. Xu, Q. Hu, S. Bai, et al., "Rational Molecular Passivation for High-Performance Perovskite Light-Emitting Diodes," *Nature Photonics* 13, no. 6 (2019): 418–424.

12. H. Zhou, Y. Ma, Y. Wang, L. Liu, G. Cheng, and S. Chen, "Cs-TFSI-Modified PEDOT:PSS Interface Engineering for High-Performance Sky-Blue Perovskite Light-Emitting Diodes: Achieving Optimal Energy Alignment and Defect Suppression," *ACS Applied Electronic Materials* 7, no. 15 (2025): 6943–6951.

13. B. Chen, C. Peng, R. Guo, et al., "Dual-Function Self-Assembled Molecules as Hole-Transport Layers for Thermally Evaporated High-Efficiency Blue Perovskite Light-Emitting Diodes," *Advanced Materials* 37, no. 3 (2025): 2411451.

14. S. Aftab, Z. Ali, M. I. Hussain, et al., "Perovskite Quantum Dots: Fabrication, Degradation, and Enhanced Performance Across Solar Cells, Optoelectronics, and Quantum Technologies," *Carbon Energy* 7, no. 9 (2025): 70018.

15. T. Fang, T. T. Wang, X. S. Li, Y. H. Dong, S. Bai, and J. Z. Song, "Perovskite QLED with an External Quantum Efficiency of Over 21% by Modulating Electronic Transport," *Science Bulletin* 66, no. 1 (2021): 36–43.

16. Y. Chen, C. Yan, Z. Chen, et al., "Interfacial Coulomb-Enhanced Charge Injection for Efficient Perovskite Light-Emitting Diodes," *Materials Today Physics* 43 (2024): 101413.

17. S. Lan, B. Pan, Y. Liu, et al., "Preparation and Promising Optoelectronic Applications of Lead Halide Perovskite Patterned Structures: A Review," *Carbon Energy* 5, no. 10 (2023): 318.

18. W. Xiong, C. Zou, W. Tang, et al., "Efficient and Bright Blue Perovskite LEDs Enabled by a Carbazole-Phosphonic Acid Interface," *ACS Energy Letters* 8, no. 7 (2023): 2897–2903.

19. G. Zou, Z. Zhu, Z. Zeng, et al., "Self-Organized Carbazole Phosphonic Acid Additives at Buried Interface Enhance Efficiency of Blue Perovskite LEDs," *ACS Energy Letters* 9, no. 9 (2024): 4715–4723.

20. B. Slimi, M. Mollar, I. Ben Assaker, A. Kriaa, R. Chtourou, and B. Marí, "Synthesis and Characterization of Perovskite $FAPbBr_{3-x}I_x$ Thin Films for Solar Cells," *Monatshefte für Chemie – Chemical Monthly* 148 (2017): 835–844.

21. F. Zhang, B. Yang, K. Zheng, et al., "Formamidinium Lead Bromide ($FAPbBr_3$) Perovskite Microcrystals for Sensitive and Fast Photodetectors," *Nano-Micro Letters* 10, no. 3 (2018): 43.

22. K. Y. Jang, S. Y. Hwang, S.-J. Woo, et al., "Efficient Deep-Blue Light-Emitting Diodes Through Decoupling of Colloidal Perovskite Quantum Dots," *Advanced Materials* 36, no. 39 (2024): 2404856.

23. X. Zhang, S. Ding, Z. Tang, et al., "Nanostructured Materials for Next-Generation Display Technology," *Nature Reviews Electrical Engineering* 2, no. 4 (2025): 263–276.

24. Z. Xu, X. Sun, W. Hui, et al., "Optimizing Molecular Packing and Interfacial Contact via Halogenated N-Glycidyl Carbazole Small Molecules for Low Energy Loss and Highly Efficient Inverted Perovskite Solar Cells," *Angewandte Chemie International Edition* 64, no. 26 (2025): 202503008.

25. J. H. Li, L. M. Xu, T. Wang, et al., "50-Fold EQE Improvement up to 6.27% of Solution-Processed All-Inorganic Perovskite $CsPbBr_3$ QLEDs via Surface Ligand Density Control," *Advanced Materials* 29 (2017): 1603885.

26. J.-N. Yang, Z.-Y. Ma, J.-D. Luo, et al., "Pseudohalogen Resurfaced $CsPbBr_3$ Nanocrystals for Bright, Efficient, and Stable Green-Light-Emitting Diodes," *Nano Letters* 23, no. 8 (2023): 3385–3393.

27. P. Pahner, H. Kleemann, L. Burtone, et al., "Pentacene Schottky Diodes Studied by Impedance Spectroscopy: Doping Properties and Trap Response," *Physical Review B* 88, no. 19 (2013): 195205.

28. Q. Zhao, H. Li, X. Zhang, S. Yu, S. Wang, and G. Sun, "Platinum In-Situ Catalytic Oleylamine Combustion Removal Process for Carbon Supported Platinum Nanoparticles," *Journal of Energy Chemistry* 41 (2020): 120–125.

29. D. Shi, V. Adinolfi, R. Comin, et al., "Low Trap-State Density and Long Carrier Diffusion in Organolead Trihalide Perovskite Single Crystals," *Science* 347, no. 6221 (2015): 519–522.

30. M. S. Kim, P. Sadhukhan, and J. M. Myoung, "High-Performance Blue Perovskite Films and Micro-Arrays for Light-Emitting Diodes with Ionic Liquid Interlayer," *Advanced Functional Materials* 34, no. 1 (2024): 2309436.

31. B. Ai, C. Liu, Z. Deng, J. Wang, J. Han, and X. Zhao, "Low Temperature Photoluminescence Properties of $CsPbBr_3$ Quantum Dots Embedded in Glasses," *Physical Chemistry Chemical Physics* 19, no. 26 (2017): 17349–17355.

32. T. J. Savenije, C. S. Ponseca, L. Kunneman, et al., "Thermally Activated Exciton Dissociation and Recombination Control the Carrier Dynamics in Organometal Halide Perovskite," *The Journal of Physical Chemistry Letters* 5, no. 13 (2014): 2189–2194.

33. L. Zhou, J.-F. Liao, Y. Qin, et al., "Activation of Self-Trapped Emission in Stable Bismuth-Halide Perovskite by Suppressing Strong Exciton–Phonon Coupling," *Advanced Functional Materials* 31, no. 31 (2021): 2102654.

34. J. Zhang, D. Zhang, X. Zhou, et al., "In-Situ Surface Repair of $FAPbBr_3$ Quantum Dots Toward High-Performance Pure-Green Perovskite Light-Emitting Diodes," *Nano Letters* 24, no. 39 (2024): 12196–12203.

35. Q. Wang, K. Wang, C. Yan, et al., "Molecularly Understanding and Regulating Carrier Injection Behavior of ETL/Perovskite Towards High Performance PeLEDs," *Chemical Engineering Journal* 456 (2023): 141077.

36. C. Yan, X. Zeng, Q. Wang, et al., "Unraveling Hole Interlayer-Dependent Interfacial Energetics of LEDs," *Nano Energy* 102 (2022): 107621.

21951071, 2026, 38, Downloaded from https://advanced.onlinelibrary.wiley.com/doi/10.1002/adom.71833 by Jilin University, Wiley Online Library on [07/11/2026]. See the Terms and Conditions (https://onlinelibrary.wiley.com/terms-and-conditions) on Wiley Online Library for rules of use; OA articles are governed by the applicable Creative Commons License

37. X. Peng, X. Yang, D. Liu, et al., "Targeted Distribution of Passivator for Polycrystalline Perovskite Light-Emitting Diodes with High Efficiency," *ACS Energy Letters* 6, no. 12 (2021): 4187–4194.

38. X. Xiao, K. Wang, T. Ye, et al., "Enhanced Hole Injection Assisted by Electric Dipoles for Efficient Perovskite Light-Emitting Diodes," *Communications Materials* 1, no. 1 (2020): 81.

39. F. Ebadi, N. Taghavinia, R. Mohammadpour, A. Hagfeldt, and W. Tress, "Origin of Apparent Light-Enhanced and Negative Capacitance in Perovskite Solar Cells," *Nature Communications* 10, no. 1 (2019): 1574.

40. L. S. C. Pingree, M. T. Russell, T. J. Marks, and M. C. Hersam, "Field Dependent Negative Capacitance in Small-Molecule Organic Light-Emitting Diodes," *Journal of Applied Physics* 100, no. 4 (2006): 044502.

41. L. Yang and R. Bashir, "Electrical/Electrochemical Impedance for Rapid Detection of Foodborne Pathogenic Bacteria," *Biotechnology Advances* 26, no. 2 (2008): 135–150.

42. M. Bag, L. A. Renna, R. Y. Adhikari, et al., "Kinetics of Ion Transport in Perovskite Active Layers and its Implications for Active Layer Stability," *Journal of the American Chemical Society* 137, no. 40 (2015): 13130–13137.

43. S. Li, Y. Yun, W. Wei, et al., "Surface Treatment Engineering Enables Highly Efficient Perovskite Light-Emitting Diodes with Significantly Enhanced Modulation Speed," *ACS Photonics* 11, no. 11 (2024): 4716–4724.

44. T.-H. Han, K. Y. Jang, Y. Dong, R. H. Friend, E. H. Sargent, and T.-W. Lee, "A Roadmap for the Commercialization of Perovskite Light Emitters," *Nature Reviews Materials* 7, no. 10 (2022): 757–777.

45. Y. Z. Jiang, C. C. Qin, M. H. Cui, et al., "Spectra Stable Blue Perovskite Light-Emitting Diodes," *Nature Communications* 10 (2019): 1868.

46. L. Pan, X. Zeng, Y. Qu, et al., "Bidirectional Inhibiting Interfacial Ion Migration in the Inorganic Hole Transport Layer for Perovskite Light-Emitting Diodes," *Small* 20, no. 48 (2024): 2405528.

Supporting Information

Additional supporting information can be found online in the Supporting Information section.

Supporting File: adom71833-sup-0001-SuppMat.docx.

21951071, 2026, 38, Downloaded from https://advanced.onlinelibrary.wiley.com/doi/10.1002/adom.71833 by Jilin University, Wiley Online Library on [07/11/2026]. See the Terms and Conditions (https://onlinelibrary.wiley.com/terms-and-conditions) on Wiley Online Library for rules of use; OA articles are governed by the applicable Creative Commons License